RSC Advances

This is an *Accepted Manuscript*, which has been through the Royal Society of Chemistry peer review process and has been accepted for publication.

Accepted Manuscripts are published online shortly after acceptance, before technical editing, formatting and proof reading. Using this free service, authors can make their results available to the community, in citable form, before we publish the edited article. This *Accepted Manuscript* will be replaced by the edited, formatted and paginated article as soon as this is available.

You can find more information about *Accepted Manuscripts* in the Information for Authors.

Please note that technical editing may introduce minor changes to the text and/or graphics, which may alter content. The journal's standard Terms & Conditions and the Ethical guidelines still apply. In no event shall the Royal Society of Chemistry be held responsible for any errors or omissions in this *Accepted Manuscript* or any consequences arising from the use of any information it contains.

ROYAL SOCIETY OF CHEMISTRY

www.rsc.org/advances

Structure and Electrical Properties of Tetragonal Tungsten Bronze $Ba_2CeFeNb_4O_{15}$

Hongqiang Ma[a], Kun Lin[a], Laijun Liu[c], Baoling Yang[a], Yangchun Rong[a], Jun Chen[a] , Jinxia Deng[a,b], Shogo Kawaguchi[d], Kenichi Kato[e], Xianran Xing*[,a]

[a] *Department of Physical Chemistry,* [b] *Department of Chemistry, University of Science and Technology Beijing, Beijing 100083, China*

[c] *State Key Laboratory Breeding Base of Nonferrous Metals and Specific Materials Processing, Guilin University of Technology, Giulin 541004, China*

[d] *Japan Synchrotron Radiation Research Institute (JASRI)1-1-1, Kouto, Sayo-cho, Sayo-gun, Hyogo 679-5198, Japan*

[e] *RIKEN SPring-8 CenterSayo, Hyogo 679-5148, Japan*

Corresponding author

Department of Physical Chemistry, University of Science and Technology Beijing, Beijing 100083, China

Tel: + 86-10-62334200

Fax: + 86-10-62332525

*e-mail address: xing@ustb.edu.cn

RSC Advances Accepted Manuscript

Abstract

The crystal structure and electrical microstructure of a tetragonal tungsten bronze (TTB) ceramic, $BaCeFeNb_4O_{15}$ (BCFN), were investigated by high-resolution synchrotron X-ray powder diffraction (SPD), selected area electron diffraction (SAED), and AC impedance spectroscopy. The SPD and SAED reveal the BCFN has a tetragonal structure with space group *P4/mbm*, and includes an incommensurate modulated behavior. Impedance and AC conductivity tests in the range of 200-360 °C suggest a thermally activated electrical behavior which originates from both the bulk and the grain boundary elements of the ceramics. The dielectric relaxation in the grain boundaries is due to the trap-controlled ac conduction around doubly ionized oxygen vacancies while the relaxation of the bulks may be associated with the localized electron hopping between the transition-metal ions. These results could be helpful in understanding the electrical conduction and relaxation processes in Fe-containing TTB-type oxides.

RSC Advances Accepted Manuscript

1. Introduction

Tetragonal tungsten bronze (TTB) type compounds are a big family of functional materials consisting of corner-sharing octahedra layers. The general composition of TTB-type structures can be formulated as $(A2)_4(A1)_2(C)_4(B1)_2(B2)_8O_{30}$, where A1, A2, and C are quadrangular, pentagonal, and triangular tunnels respectively.[1] B1 and B2 are the octahedral sites, (see Fig. 1). Generally, A1 and A2 sites can be fully or partially occupied by larger cations, like alkaline, alkaline earth, rare earth, bismuth or lead;[2,3] while small C sites can be filled with very small ions such as Li^+ ions but are typically vacant.[4] This variety of the instinct crystalline sites provides degrees of freedom for tuning the chemical composition and, thus, offering flexibility of properties.[5-8] For example, in the family of $Ba_2REFeNb_4O_{15}$ (RE = rare earth atoms) ceramics, the quadrangular tunnels (A1) play an important role in the dielectric behaviors.[9-11] The incorporation of large cations, such as La^{3+}, Pr^{3+} etc., into the A1 sites, leads to relaxor properties, whereas the introduction of smaller one (Nd^{3+}, Sm^{3+}, Eu^{3+}, Gd^{3+}) induces classical ferroelectric behaviors. The incorporation of Fe ion in the B sites for electroneutrality seems not trigger an anticipatory multiferroic property in $Ba_2REFeNb_4O_{15}$ since the parasitic phase $BaFe_{12}O_{19}$ is responsible for the magnetic properties.[12-14] But it could restrain the cooperative displacements as well as the polar domain formation, which has significant influence on their dielectric behavior, for example, in $Ba_2LaFeNb_4O_{15}$ ceramics with smaller permittivity compared with $Ba_2LaTi_2Nb_3O_{15}$.[15] Unfortunately, the detailed charge transport mechanism is still unclear.

It is known that polarizability along with conductivity arises when multi-valence cations (such as Fe, Mn, Cu) are introduced in pervoskite or other oxides.[16] The polyvalent Fe ions coupled with the oxygen vacancies generated in the high temperature sintering process would likely play a

RSC Advances Accepted Manuscript

predominant role in determining the electrical and dielectric behaviors.[17,18] For example, in the case of (La, Mg)-doped $BiFeO_3$, electrons hopping between Fe^{2+}-Fe^{3+} and single-charged oxygen vacancies ($V_o^{\cdot}$) make contribution to dielectric response of grains and grain boundaries, respectively.[18] Similarly, O. Raymond and his co-workers investigated the ferroelectromagnetic $Pb(Fe_{0.5}Nb_{0.5})O_3$ ceramics, and concluded that the presence of Fe^{2+} fundamentally contributes to the nonlocalized conduction and the oxygen vacancies are responsible for the dielectric relaxation process.[19] Actually, significant dielectric losses can be observed when Fe ions are introduced in the TTB compounds at room temperature (RT),[12,20,21] which may be associated with nonlocalized conduction. For a better understanding of the physical nature of the electrical properties and relaxation processes for Fe-containing TTBs, we designed and synthesized a new compound, $Ba_2CeFeNb_4O_{15}$ (BCFN). The crystal structure was investigated by high-resolution synchrotron X-ray powder diffraction (SPD) and selected area electron diffraction (SAED) at RT. The electrical microstructure of the ceramics (above RT) was characterized by impedance spectroscopy. We found that the as-synthesized BCFN adopts an incommensurate modulated structure at RT, and that the trap-controlled ac conduction around doubly ionized oxygen vacancies was responsible for the dielectric relaxation in the grain boundaries while the relaxation of the bulks may be related to the localized electron hopping between the Fe^{2+} - Fe^{3+}.

2. Experimental Section

Polycrystalline specimens of $Ba_2CeFeNb_4O_{15}$ were synthesized by a solid-state route using $BaCO_3$ (99%), Fe_2O_3 (99%), Nb_2O_5(99.99%) and CeO_2 (99.9%) as starting materials. $BaCO_3$ and Fe_2O_3 were purchased from Xilong Chemical Co., Ltd. (Guangzhou, China), and Nb_2O_5 and CeO_2 were supplied by Sinopharm Chemical Reagent Co., Ltd. (Shanghai, China). The ball-milled powders

RSC Advances Accepted Manuscript

according to aimed stoichiometry were calcined at 800 °C for 4 h. The calcined products were ball-milled again for 4 h and then pressed into pellets uniaxially. The pellets were fired at 1320 °C for 6 h. High-angular resolution synchrotron X-ray powder diffraction (SPD) data were collected using a Debye–Scherrer camera with an imaging plate on beam line BL02B2 at SPring-8, Japan (RT; wavelength = 0.5001 Å). The structure was refined by Rietveld method using Jana2006 software. For SAED study, a pellet specimen was pretreated with ion-beam thinning. SAED were observed by JEOL JEM-2010 at the accelerating voltage of 200 kV. AC impedance spectroscopy measurements from 200 °C to 360 °C in air were carried out with a Solartron SI 1260 impedance analyzer over the frequency range 0.5 Hz to 100 kHz, with an oscillator voltage of 1000 mV. Before measurements, silver paste was coated onto both sides of the polished pellet as an electrode and fired at 650 °C for 30 min. The complex impedance data were corrected for sample geometry (thickness/area of pellet) and analyzed using Zview software.

3. Results and discussion

3.1. Crystal structure of $Ba_2CeFeNb_4O_{15}$

Preliminary LeBail fitting carried out against the SPD data shows BCFN is a tetragonal phase with a = 12.491(2) Å, c = 3.926(2) Å. Space group *P*4*bm* (No. 100) and *P*4/*mbm* (No. 127) were assigned on the basis of the systematic absences. However, the non-centrosymmetric space group P4bm was abandoned since the second harmonic generation (SHG) signal was not detected under a picosecond Laser. The starting *P*4/*mbm* model reported previously in $Ba_2LaTi_2Nb_3O_{15}$ at 400 K[22] was used for refinements of the SPD pattern (see Fig. 2 and Table 1). The big Ba atoms are prior to occupy A2 (pentagonal) sites due to the negative convergence in A1 (quadrangle) sites. Then the Ce atoms reside in the A1 sites. Refinement for the occupancy of Ba and Ce atoms

RSC Advances Accepted Manuscript

respectively did not improve the fit significantly, so the barium, cerium and niobium/iron were fixed to the nominal stoichiometry. Iron and niobium ions were provisionally arranged at 2c and 8j sites (corresponding B1 and B2 respectively), respectively. Then the cross-substitutions of Nb and Fe in the octahedral sites were also tested. The value of χ^2 decreased from 2.87 to 2.69.The occupancies of Nb in B1 and B2 were ~0.804 and ~0.799 respectively, indicating Fe and Nb are almost statistically distributed in the octahedral sites. The final refinement agreement factors were listed in Table 1.

Fig 3 shows the selected area electron diffraction pattern of BCFN crystals taken along the [114] and [116] zone axes at RT. Extra spots along [110] direction corresponding to the first-order incommensurate reflections are observed in the TTB paraelectric phase. The modulation can be characterized by the vector: $\boldsymbol{q} \approx 0.286(\boldsymbol{a}^*+\boldsymbol{b}^*) + 0.5\boldsymbol{c}^*$. The weak stripes lying between the two strong reflections along [110] direction may be the second-order satellite reflections of the incommensurate spots in Fig 4(b). Inspection of the U_{iso} values in Table 1 shows somewhat large values for oxygen atoms suggesting that the modulation may have a strong influence on the anionic sublattice.

3.2. Impedance and modulus analysis

The charge transport mechanism in polycrystalline device materials commonly exhibits several components such as grain boundary, bulk and electrode interface contributions, which can be separated and quantitatively determined by AC impedance spectroscopy measurements.[23] AC impedance data in the form of a complex plane plot in Fig. 4 shows two semicircles over the measured temperature range, indicating BCFN pellet with heterogeneous electrical microstructure. For the data measured at 240 °C the capacitances ~24.6 pF/cm and 23.6 nF/cm were obtained by

RSC Advances Accepted Manuscript

the relationship $\omega RC = 1$ at the two semicircle arcs maximum (where ω is angular frequency corresponding to the maximum Z''), which indicates that the two contributions are from bulks (left) and grain boundaries (right), respectively.[23,24]

Fig. 5(a) shows the variation of imaginary part of the impedance (Z'') with frequency at different temperatures for BCFN. It can be observed that two peaks appear below 320 °C indicative of the presence of at least two relaxation processes in bulks and grain boundaries, respectively. The two peaks move to higher frequency as temperature rises. This behavior suggests a decrease in the relaxation time with increasing temperature, and depicts a thermal activated electrical response. This possibly originates from the presence of space charge at grain boundaries.[25,26] The merging of all the curves above 50 kHz and the decrease in the height of the peaks indicate a possible release of the space charge. The impedance data are rationalized using modified KWW (Kohlrausch–Williams–Watts) function as proposed by Bergman[27]

$$Z''=Z''_{max}/\left[1-\beta+\left(\frac{\beta}{1+\beta}\right)\left(\beta\left(\frac{\omega_{max}}{\omega}\right)+\left(\frac{\omega}{\omega_{max}}\right)^{\beta}\right)\right] \quad (1)$$

Where Z''_{max} and ω_{max} define the peak value of Z'' and the corresponding angular frequency, respectively. β is the stretching factor ($0 < \beta < 1$) which decreases with an increase in the width of the relaxation time distribution. The data are well fitted except those in the low frequencies (< 500 Hz). The deviations from the fitted curves in the low frequencies can be related to the electrode contributions. Activation energies of the bulk E_b = 0.46 eV and grain boundary E_{gb} =0.71 eV were obtained from the fitting data above using Arrhenius formula $f_{max} = f_o \exp(-E_a/kT)$ where f_{max} $(\omega_{max}/2\pi)$ is relaxation frequency, f_o is the pre-exponential factor, k is the Boltzmann constant and T is absolute temperature (see Fig. 5b).

The imaginary part of electric modulus, M'', has been invoked to understand the bulk response of

RSC Advances Accepted Manuscript

the samples, since the maxima of *M"* spectra are dominated by components with smallest capacitance. Fig. 6(a) shows frequency dependence of *M"* at various temperatures. It can be noted that a strong relaxation peak exists in high frequency range (> 1500Hz) with the peak M''_{max} shifting to higher frequencies. The solid lines represent the theoretical adjustment with the modified KWW function. For the stretching factor $\beta = 1$ we have an ideal Debye relaxation. Thus the β obtained to be 0.92 indicates a slight departure from the ideal Debye behavior in the bulk. Fig. 6(b) shows that the relaxation frequency f_{Mmax} (corresponding to M''_{max}) also obeys the Arrhenius formula. The corresponding activation energy E_a = 0.45 eV is found to be close to the activation energy E_b (0.46 eV) corresponding to *Z"* spectra. The comparable values of activation energies for *Z"* (representing dielectric relaxation) and *M"* (representing delocalized conduction) suggest that the relaxation and conduction processes are attributed to the same type of charge carriers. We have scaled each *M"* by M''_{max} and each frequency by f_{max} for different temperatures in Fig. 6(c). All the peaks at different the temperatures overlapped into a single master curve except on the high frequency tail which is possibly due to the resonance of the measuring leads.[28] This indicates that all dynamic processes of the charge carriers in the bulk are nearly temperature independent and exhibit the same activation energy.[18,29]

3.3. Conductivity analysis

AC conductivity (σ') of the sample was calculated from the complex impedance data using the relation

$$\sigma' = Z'/(Z'^2 + Z''^2) \quad (2)$$

where *Z'* and *Z"* (unit, Ωcm) were corrected for overall pellet geometry. Fig. 7(a) shows the AC conductivity plots as a function of frequency at different temperatures. The curves tend to flatten

RSC Advances Accepted Manuscript

with increasing temperature in the low frequency regions, which is related to DC conduction behavior. The conductivity shows a step-like behavior below 320 °C suggesting a multiple relaxation process. These step-like dispersion was analyzed using Jonshcer' power law[30]

$$\sigma' = \sigma_{dc} + A\omega^n \quad (3)$$

where σ_{dc} defines the DC conductivity, A is temperature dependent pre-exponential term and n is frequency exponent representing the interaction of the mobile carriers.[19] The frequency independent plateau in 100-10 kHz range denotes the bulk dc conduction (σ_b), while dispersion and another plateau in the lower frequency region correspond to relaxation behavior in grain boundary and total DC conduction (σ_{total}), respectively. The grain boundary DC conductivity can be obtained by relation $1/\sigma_{gb}=1/\sigma_{total}-1/\sigma_b$, as the small contributions leads and electrode have been ignored. Fig. 7(b) shows the Arrhenius plots of DC conductivity for bulk and grain boundary. The values of the activation energy for bulk conduction (E_b) and grain boundary conduction (E_{gb}) are 0.50 eV and 0.72 eV, respectively, which are very close to the values of activation energy for relaxation.

Actually, during sintering process at high temperatures with low oxygen partial pressure, the oxygen vacancies could be generated easily by the loss of oxygen from the crystal lattice, and the ionization of oxygen will create conducting electrons,

$$V_o \Leftrightarrow V_o^{\cdot} + e' \quad (4a)$$

$$V_o^{\cdot} \Leftrightarrow V_o^{\cdot\cdot} + e' \quad (4b)$$

or these electrons might be bonded to Fe^{3+} ions in the form of

$$Fe^{3+} + e' \Leftrightarrow Fe^{2+} \quad (5)$$

These electrons may be trapped by Fe^{3+} and oxygen vacancies, forming color centers, which can

RSC Advances Accepted Manuscript

be thermally activated easily becoming conducting electrons.[31] The UV-vis absorbance spectra and XPS data (see Fig. S3, S4) confirmed the existence of Fe^{2+} and oxygen vacancies in the as-sintered pellets.

The dipole-type polarization in the samples was excluded due to the almost same activation energy for electrical conduction and dielectric relaxation.[31,32] The observed activation energies for the electrical conduction and dielectric relaxation in grain boundaries are close to 0.7 eV, which suggests that the conduction carriers are electrons from the second ionization of oxygen vacancies $V_o^{\cdot\cdot}$. The trap-controlled ac conduction around doubly ionized oxygen vacancies contributes to the dielectric relaxation (similar to the polaron behavior observed in some oxides),[31] while the long distance movement of these electrons contributes to the electrical conduction. It is noteworthy that the fitting activation energy E_a (~0.45 eV) for bulk relaxation was slightly larger than reported value of 0.29 eV in $Bi_{0.85}Nd_{0.15}FeO_3$[33], 0.325eV in $BiFeO_3$[34], 0.38 eV in $Sr(Fe_{0.5}Nb_{0.5})O_3$[35], indicative of two-site electron hopping between the transition-metal ions (Fe, Nb).[20] XPS studies on the $Ba_2REFeNb_4O_{15}$ single crystals by Josse and co-workers[16] have shown that the reduction of niobium has an association effect on the reduction of iron in reduction phenomenon. The lower concentration of Fe atoms in octahedra (25% occupation) and the statistical distributions of Fe and Nb atoms on the octahedral sites may raise the enthalpies for electron hopping as a result of larger activation energy. In addition, the appreciable DC conductivity at high temperatures and semiconducting behavior with a room temperature conductivity (> 1×10^{-8} S/cm, not shown) may endow the BCFN compound with potential applications in thermoelectric materials.[36]

4. Conclusions

In this work, the structure of a TTB compound, $BaCeFeNb_4O_{15}$, was investigated by synchrotron

RSC Advances Accepted Manuscript

radiation and selected area electron diffraction. The as-synthesized BCFN ceramic was a paraelectric phase at RT and displays an incommensurate modulation with $\boldsymbol{q} \approx 0.286(\boldsymbol{a}^*+\boldsymbol{b}^*) + 0.5\boldsymbol{c}^*$. The impedance spectroscopy of polycrystalline $Ba_2CeFeNb_4O_{15}$ was investigated in the range of 200-360 °C. Activation energies of the bulk (~0.45 eV) and grain boundary (~0.70 eV) were obtained from the thermally activated Arrhenius fit on impedance and AC conductivity data. The scaling behavior of the imaginary part of electronic (*M"*) suggests that the relaxation process and dynamics are nearly temperature independent. The introduction of mixed-valence cations (Fe) in TTBs could help understanding the origins of leakage current, polarization fatigue and provide an approach to explore thermistor and thermoelectric materials in TTB family.

Acknowledgements

This work was supported by the National Natural Science Foundation of China (grant no. 91022016, 91422301, and 21231001), the Program for Changjiang Scholars and the Innovative Research Team in University (IRT1207), and the Fundamental Research Funds for the Central Universities, China (Grant No. FRF-SD-13-008A).

References

1 P. B. Jamieson, S. C. Abrahams, J. L. Bernstein, *J. Chem. Phys.*,1968, **48**, 5048−5056.

2 Simon, and J. Ravez, *C. R. Chim.*, 2006, **9**, 1268–1276.

3 K. Lin, H. Wu, F. Wang, Y. Rong, J. Chen, J. Deng, R. Yu, L. Fang, Q. Huang, and X. Xing, *Dalton Trans*., 2014, **43**, 7037−7043.

4 K. Lin, Y. Rong, H. Wu, Q. Huang, L. You, Y. Ren, L. Fan, J. Chen, and X. Xing, *Inorg. Chem.*, 2014, **53**, 9174–9180.

5 V. V. Shvartsman, and D. C. Lupascu. *J. Am. Ceram. Soc.*, 2012, **95**, 1–26.

6 Kaiser, J. L. Bradley, P. R. Slater, and J. T. S. Irvine, *Solid State Ionics*, 2000, **135**, 519–524.

7 H. Ma, K. Lin, L. Fan, Y. Rong, J. Chen , J. Deng, L. Liu，S. Kawaguchi, K. Kato, and X. Xing. *RSC. Adv*., 2015, **5**, 71890–71895.

RSC Advances Accepted Manuscript

[8] R. R. Neurgaonkar, J. R. Oliver, W. K. Cory, L. E. Cross, and D. Viehland, *Ferroelectrics*, **160**, 1994, 265–276.

[9] M. Josse, O. Bidault, F. Roulland, E. Castel, A. Simon, D. Michau, R. Von der Mühll, O. Nguyen, and M. Maglione, *Solid State Sci.*,2009, **11**, 1118–1123.

[10] Hu, X. Peng, C. Li, L. Fang, and L. Liu, *Ferroelectrics*, 2010, **404**, 33–38.

[11] M. Kinka, M. Josse, E. Castel, S. Bagdzevicius, V. Samulionis, R. Grigalaitis, J. Banys, and M. Maglione, *IEEE Trans. Ultrason. Ferroelectr. Freq. Control*, 2012, **59**, 1879–1882.

[12] M. Albino, P. Veber, E. Castel, M. Velázquez, K. Schenk, G. Chapuis, M. Lahaye, S. Pechev, M. Maglione, and M. Josse, *Eur. J. Inorg. Chem.*, 2013, **15**, 2817–2825.

[13] E. Castel, M. Josse, F. Roulland, D. Michau, L. Raison, and M. Maglione, *J. Magn. Magn. Mater.*, 2009, **321**, 1773–1777.

[14] E. Castel, P. Veber, M. Albino, M. Velázquez, S. Pechev, D. Denux, J.P. Chaminade, M. Maglione, and M. Josse, *J. Cryst. Growth*, 2012, **340**, 156–165.

[15] E. E. McCabe, and A. R. West, *J. Solid. State. Chem.*, 2010, **183**, 624–630.

[16] M. Maglione, and M. A. Subramanian, *Appl. Phys. Lett.*,2008, **93**, 032902, 3pp.

[17] W. Bai, G. Chen, J. Y. Zhu, J. Yang, T. Lin, X. J. Meng, X. D. Tang, C. G. Duan, and J. H. Chu, *Appl. Phys. Lett*., 2012, **100**, 082902, 4pp.

[18] Q. Ke, X. Lou, Y. Wang, and J. Wang, *Phys. Rev. B: Condens. Matter Mater. Phys.*, 2010, **82**, 024102, 7pp.

[19] Raymond, R. Font, N. Suárez-Almodovar, J. Portelles, and J. M. Siqueiros, *J. Appl. Phys*., 2005, **97**, 084108, 8pp.

[20] M. Albino, P. Veber, S. Pechev, C. Labrugere, M. Velazquez, M. Maglione, and M. Josse, *Cryst Growth Des.*, 2014, **14**, 500–512.

[21] Y. J. Wu, Z. J. Hong, Y. Q. Lin, S. P. Gu, X. Q. Liu, and X. M. Chen , *J. Appl. Phys*., 2010, **108**, 014111, 5pp.

[22] G. C. Miles, M. C. Stennett, I. M. Reaney, and A. R. West, *J. Mater. Chem.*, 2005, **15**, 798−802.

[23] J. T. S. Irvine, D. C. Sinclair, A. R. West, *Adv. Mater.*, 1990, **2**, 132−138.

[24] Peláiz-Barranco, M. P. Gutiérrez-Amador, A. Huanosta, and R. Valenzuela, *Appl. Phys. Lett.*, 1998, **73**, 2039–2041.

RSC Advances Accepted Manuscript

[25] M. M. Costa, G. F. M. Pires, Jr., A. J. Terezo, M. P. F. Graca, and A. S. B. Sombra, *J. Appl. Phys*., 2011, **110**, 034107, 7pp.

[26] R. Tang, C. Jiang, J. Jian, Y. Liang, X. Zhang, H. Wang, and H. Yang, *Appl. Phys. Lett.*, 2015 **106**, 022902, 5pp.

[27] R. Bergman, *J. Appl. Phys*., 2000, **88**, 1356-1365.

[28] A. Srivastava, A. Garg, and F. D. Morrison, *J. Appl. Phys*., 2009, **105,** 054103, 6pp.

[29] S. Saha, T. P. Sinha, *Phys. Rev. B: Condens. Matter Mater. Phys.*, 2002, **65**, 134103, 7pp.

[30] K. Jonscher, *Nature*, 1977, **267**, 673–679.

[31] Ang, Z. Yu, and L. E. Cross, *Phys. Rev. B: Condens. Matter Mater. Phys.*,2000, **62**, 228−236.

[32] Morii, H. Kawano, I. Fujii, T. Matsui, and Y. Nakayama, *J. Appl. Phys.*, 1995, **78**, 1914–1919.

[33] Kalantari, I. Sterianou, S. Karimi, M. C. Ferrarelli, S. Miao, D. C. Sinclair, and I. M. Reaney, *Adv. Funct. Mater.*, 2011, **21**, 3737–3743.

[34] S. Hunpratub, P. Thongbai, T. Yamwong, R. Yimnirun, and S. Maensiri, *Appl. Phys. Lett.*, 2009, **94,** 062904, 3pp.

[35] Y. Y. Liu, X. M. Chen, X. Q. Liu and L. Li, *Appl. Phys. Lett.*, 2007, **90**, 262904, 3pp.

[36] S. Lee, R. H. T. Wilke, S. T. McKinstry, S. Zhang, and C. A. Randall, *Appl. Phys. Lett.,* 2010, **96,** 031910, 3pp.

RSC Advances Accepted Manuscript

Figure Captions

Fig. 1 Schematic structure of tetragonal tungsten bronze BCFN in [001] and [010] projection with space group *P*4*/mbm*.

Fig. 2 Rietveld fit pattern for high-resolution synchrotron X-ray powder diffraction (SPD) data of BCFN collected at RT with space group *P*4*/mbm*.

Fig. 3 SAED patterns taken along the (a) [114], (b) [116] zone axes at RT. The arrows highlight the satellites of the incommensurate modulation.

Fig. 4 Nyquist plots of the impedance of the BCFN obtained at different temperatures; the inset shows the high-temperature data on an expanded scale. The solid lines represent the fit of Z* data using the equivalent software.

Fig. 5(a) Frequency dependence of *Z"*(imaginary) at several measurement temperatures for BCFN pellet, and the solid lines represent the fit of Z" data to the modified KWW function; (b) The Arrhenius plots shows the dependence of f_{max}(*Z"*) vs 1000/T of BCFN.

Fig. 6(a) Imaginary part of the electric modulus, *M"* vs frequency at various temperatures. The solid lines represent the fit of *M"* data to the modified KWW function. (b) The Arrhenius plots shows the dependence of f_{max}(*M"*) vs 1000/T of BCFN. (c) Scaling behavior of *M"* by $M"_{max}$ and f_{max} at various temperatures.

Fig. 7(a) AC conductivity plots as a function of frequency at different temperatures. The dash lines represent the theoretical fits of bulk contribution to the equation (4). (b) Arrhenius plots of the DC conductivity of BCFN Pellet.

RSC Advances Accepted Manuscript

Table Captions

Table 1. The Final Refined Structural Parameters of BCFN at RT.

RSC Advances Accepted Manuscript

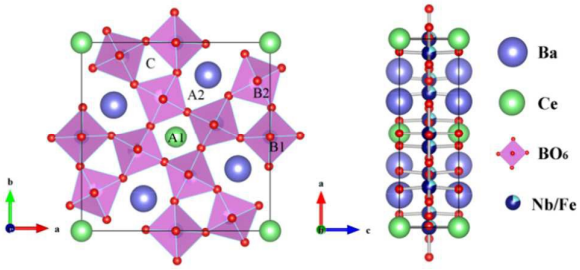

Fig. 1 Schematic structure of tetragonal tungsten bronze BCFN in [001] and [010] projection with space group *P4/mbm*.

RSC Advances Accepted Manuscript

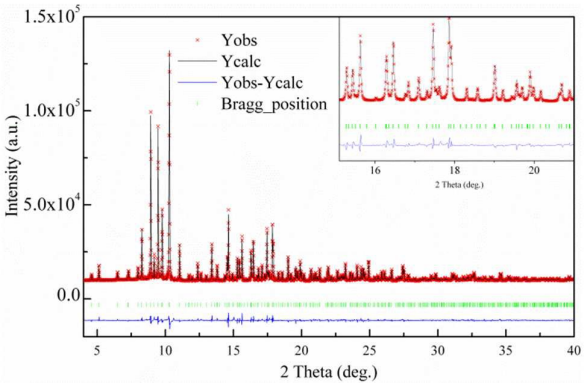

Fig. 2 Rietveld fit pattern for high-resolution synchrotron X-ray powder diffraction (SPD) data of BCFN collected at RT with space group *P*4/*mbm*.

RSC Advances Accepted Manuscript

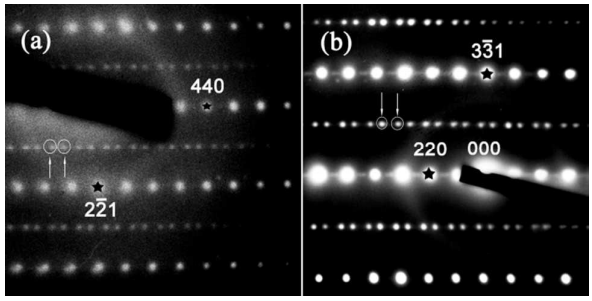

Fig. 3 SAED patterns taken along the (a) [114] and (b) [116] zone axes at RT. The arrows highlight the satellites of the incommensurate modulation.

RSC Advances Accepted Manuscript

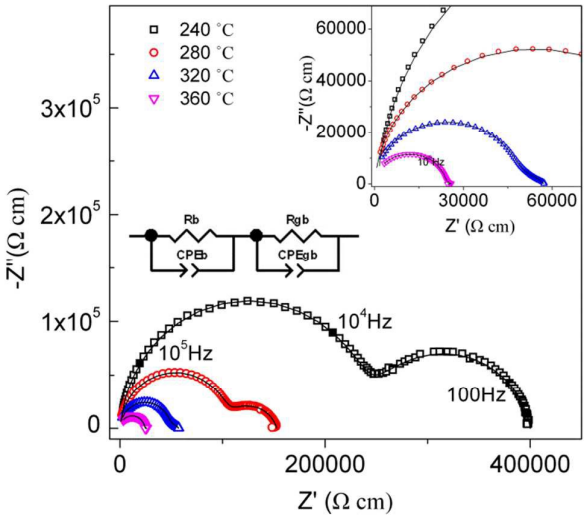

Fig. 4 Nyquist plots of the impedance of the BCFN obtained at different temperatures; the inset shows the high-temperature data on an expanded scale. The solid lines represent the fit of Z* data using the equivalent software.

RSC Advances Accepted Manuscript

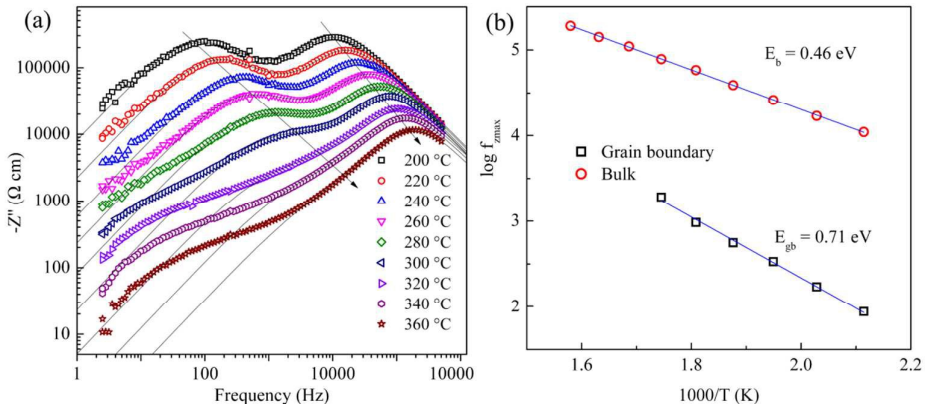

Fig. 5(a) Frequency dependence of *Z"*(imaginary) at several measurement temperatures for BCFN pellet and the solid lines represent the fit of Z" data to the modified KWW function;; (b) The Arrhenius plots shows the dependence of f_{max}(*Z"*) vs 1000/T of BCFN.

RSC Advances Accepted Manuscript

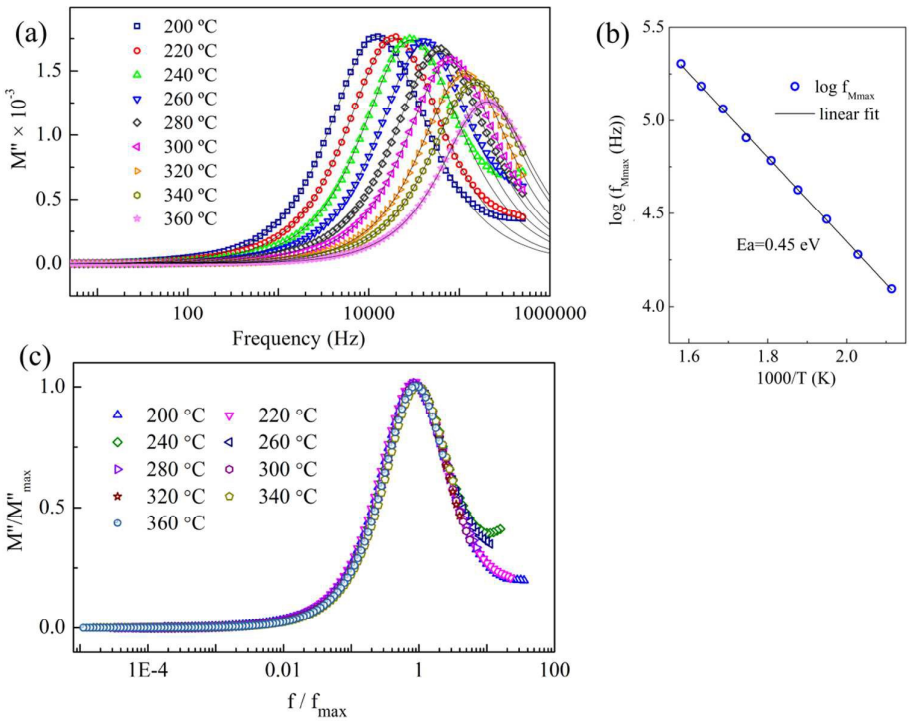

Fig. 6(a) Imaginary part of the electric modulus, *M"* vs frequency at various temperatures. The solid lines represent the fit of *M"* data to the modified KWW function. (b) The Arrhenius plots shows the dependence of $f_{max}(M")$ vs 1000/T of BCFN. (c) Scaling behavior of *M"* by $M"_{max}$ and f_{max} at various temperatures.

RSC Advances Accepted Manuscript

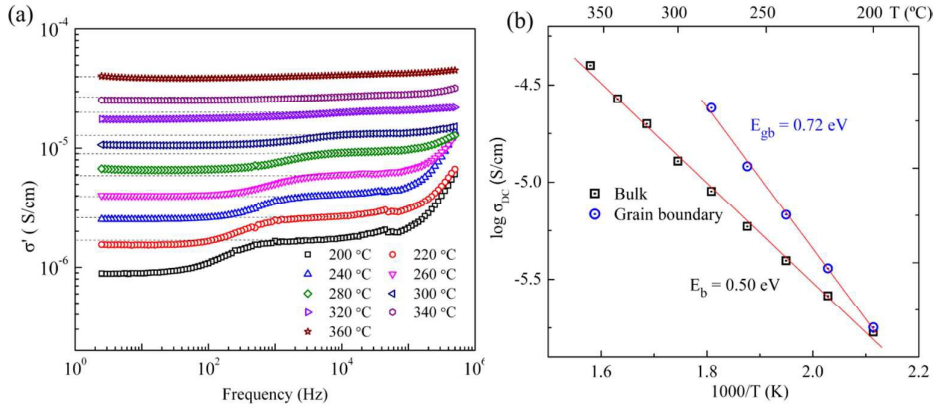

Fig. 7(a) AC conductivity plots as a function of frequency at different temperatures. The dash lines represent the theoretical fits of bulk contribution to the equation (4). (b) Arrhenius plots of the DC conductivity of BCFN Pellet.

RSC Advances Accepted Manuscript

Table 1. The Final Refined Structural Parameters of BCFN at RT

atom	Site	x	y	z	U_{iso} (Å^2)	Occupancy
Ce	2a	0	0	0	0.0141(5)	1
Ba	4g	0.1708(1)	0.6708(1)	0	0.0223(4)	1
Fe1	2c	0	0.5	0.5	0.0076(3)	0.1964(23)
Nb1	2c	0	0.5	0.5	0.0076(3)	0.8036(23)
Fe2	8j	0.0747(1)	0.2145(1)	0.5	0.0076(3)	0.2009(1)
Nb2	8j	0.0744(1)	0.2147(1)	0.5	0.0076(3)	0.7991(1)
O1	2d	0	0.5	0	0.0149(51)	1
O2	4h	0.2803(6)	0.7803(6)	0.5	0.0072(36)	1
O3	8i	0.0677(9)	0.2020(7)	0	0.0415(30)	1
O4	8j	0.3420(7)	0.0070(5)	0.5	0.0147(25)	1
O5	8j	0.1343(8)	0.0604	0.5	0.0562(41)	1

Space group *P4/mbm*, Z = 1, a = 12.4905(1) Å, c = 3.9268(1) Å

V = 612.63(3) Å^3; R_{wp}=2.37%, R_p=1.54%, χ^2 = 2.55.

RSC Advances Accepted Manuscript

Graphical Abstract:

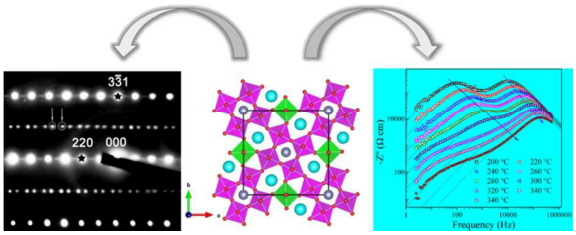

79.9×33.4 mm (700 x 700 dpi)

RSC Advances Accepted Manuscript